

# Elastic-plastic properties of mesoscale electrodeposited LIGA nickel alloy films: microscopy and mechanics

Li-Anne Liew<sup>1</sup> , David T Read<sup>1</sup> , May L Martin<sup>1</sup> , Frank W DelRio<sup>1,4</sup> , Peter E Bradley<sup>1</sup>, Nicholas Barbosa<sup>1</sup>, Todd R Christenson<sup>2</sup> and John T Geaney<sup>3</sup>

<sup>1</sup> Applied Chemicals and Materials Division, National Institute of Standards and Technology, Boulder, CO 80305, United States of America

<sup>2</sup> HT MicroAnalytical Inc, Albuquerque, NM 87109, United States of America

<sup>3</sup> US Army Combat Capabilities Development Command Armaments Center, Picatinny Arsenal, NJ 07806, United States of America

E-mail: [li-anne.liew@nist.gov](mailto:li-anne.liew@nist.gov)

Received 2 May 2020, revised 23 September 2020

Accepted for publication 14 October 2020

Published 23 November 2020



## Abstract

The elastic-plastic properties of mesoscale electrodeposited LIGA Ni alloy specimens are investigated as a function of specimen size, strain rate, and material composition. Two material compositions are studied: a high-strength fine-grained Ni-Fe alloy and a high-ductility coarse-grained Ni-Co alloy. The specimens have thicknesses of approximately 200  $\mu\text{m}$  and gauge widths ranging from 75  $\mu\text{m}$  to 700  $\mu\text{m}$ . Tensile tests are conducted at strain rates of 0.001/s and 1/s using tabletop loading apparatuses and digital image correlation (DIC) for strain measurement. For each test condition, the apparent Young's modulus, yield strength, ultimate tensile strength, and strain hardening exponent and strength coefficient are extracted from the tensile tests. The true strains to failure are also assessed from fractography. Size, rate, and composition effects are discussed. For most properties, the statistical scatter represented by the standard deviation exceeds the measurement uncertainty; the notable exceptions to these observations are the apparent Young's modulus and yield strength, where large measurement uncertainties are ascribed to common experimental factors and material microplasticity.

Keywords: LIGA, electrodeposited nickel, elastic-plastic properties, mesoscale mechanical testing, digital image correlation, strain rate

(Some figures may appear in colour only in the online journal)

## 1. Introduction

The first microelectromechanical systems (MEMS) to be widely commercialized were made of bulk single-crystal silicon and polycrystalline silicon thin films. However, in the 1980s, another major microfabrication technology emerged for manufacturing thick-film and high-aspect-ratio metal MEMS. Known as LIGA (Lithographie, Galvanoformung, Abformung), this fabrication process produces metal structural layers with thicknesses from a few micrometers to

several hundreds of micrometers and thickness-to-width ratios of up to 1000:1 [1–4]. The most common structural materials used are nickel and binary alloys of nickel. The fabricated metal components are used as MEMS devices, or as molds for polymer high-aspect-ratio devices for microfluidic applications. As such, the mechanical properties of LIGA materials have been an ongoing area of active research.

The mechanical properties of LIGA MEMS depend on the film microstructure and chemistry, test conditions, and component size. On microstructural effects, there have been many studies on the mechanical properties of electrodeposited Ni films (*e.g.* see [5, 6] and the references therein).

<sup>4</sup> Now at Sandia National Laboratories, Albuquerque, NM 8712

It has been shown that the microstructure and properties of electrodeposited Ni films, including those from the LIGA process, are sensitive to processing conditions such as plating current density, bath chemistry and agitation, pH, and temperature. For example, subsequent studies generally described an increase in ultimate tensile strength with a decrease in average grain size [7–9], with one noteworthy exception attributed to the preferred grain orientation in the film [9]. With respect to chemical composition, studies on nanocrystalline Ni-Fe alloys have reported sizeable changes in Young's modulus, yield strength, ultimate tensile strength, and fracture toughness through the inclusion of the alloy component [10–12]. With respect to test conditions, the loading rate (*i.e.* strain rate) and type (*i.e.* monotonic or cyclic) have been shown to impact the observed mechanical properties of electrodeposited Ni and Ni-Fe films; the rate dependence has been attributed to grain boundary diffusion [13] and grain boundary and dislocation interactions [14], whereas the type dependence has been ascribed to dislocation source exhaustion and cyclic hardening [15]. On component size effects, the thickness and width of specimens reported in the literature span an order of magnitude, likely leading to property variability via size-dependent effects. In fact, measurable differences in ultimate tensile strength [16] and strain hardening behavior [17] were observed with only two-fold changes in thickness or width when keeping all other factors constant, while Wang *et al* [18] observed a size effect on the Young's modulus. Given these dependencies, the wide scatter in reported values for mechanical properties of LIGA Ni and its alloys is not surprising. Also, the strain hardening of LIGA Ni alloys has received relatively less attention than other mechanical properties in the literature thus far. Thus, to further enable design and commercialization, more systematic studies on the mechanical properties are needed to elucidate and deconvolute the effects of microstructure, chemistry, test conditions, and size.

In this work, we characterized the room-temperature elastic-plastic properties of two commercially produced LIGA Ni alloys, a nanograined Ni-Fe alloy and a micrograined Ni-Co alloy, using specimens with thicknesses between 160  $\mu\text{m}$  and 190  $\mu\text{m}$  and ranging in gauge width from 75  $\mu\text{m}$  to 700  $\mu\text{m}$  at strain rates from 0.001/s to 1/s. The tensile testing approach was based on commercial macroscopic tensile testing platforms adapted for use on mesoscale specimens. Force was measured by load cells, and displacement was measured by digital image correlation (DIC) with optical microscopy, which provided the basis for engineering stress–strain curves. The apparent Young's modulus, 0.2% offset yield strength, ultimate tensile strength, strain hardening exponent and strength coefficient were determined for the two alloys, at the two strain rates, and over four specimen gauge widths, from the engineering stress–strain curves. The true strain to failure was measured via fractography with scanning electron microscopy (SEM). The chemistry and microstructure were also measured by electron dispersive spectroscopy (EDS) and focused ion beam (FIB) microscopy. Size and rate effects on each property for each alloy were identified via two-factor analysis of variables (ANOVA). In addition, the measurement uncertainties in the elastic-plastic properties, as determined by

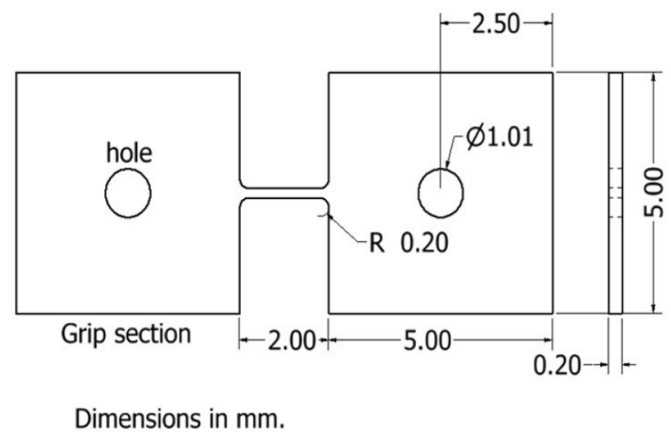


**Figure 1.** Engineering drawing for the nominal (S1) tensile test specimen. The nominal thickness was 200  $\mu\text{m}$ .

error analysis, were compared to statistical variations as represented by the standard deviations about the mean values. Please note that this paper is intended as the first part of a two-part paper, the second of which focuses on the measurement uncertainties and statistical uncertainties, and the trends with material and test condition. As such, discussion of the uncertainties in this paper is limited. The complete set of elastic-plastic properties are analyzed to deconvolute the effects of microstructure, chemistry, component size, and test conditions, thus enabling a comprehensive processing-structure-property relation for the two alloys studied.

## 2. Materials and methods

### 2.1. Specimen design, fabrication, chemistry, and microstructure

The test specimens were mesoscale (*i.e.* with smallest dimensions ranging from tens to hundreds of micrometers) and designed to encompass a wide range of component sizes. There were four designs, denoted S1 to S4. Gauge widths ranged from 75  $\mu\text{m}$  to 700  $\mu\text{m}$ , gauge lengths ranged from 1.2 mm to 3 mm, and the thickness was nominally 200  $\mu\text{m}$ . Figure 1 illustrates the S1 design, which is also referred to as the ‘nominal’ design which has a square cross-section. The S2, S3, and S4 designs have rectangular cross-sections. The specimen geometries were roughly scaled-down versions of those in ASTM E-8 [19] for pin-loaded specimens, but adaptations were made to accommodate handling at the smaller sizes. For example, the grip section widths and the fillet radii differed from ASTM E-8 proportions, but the width-to-thickness ratio of at least 0.78 criterion is met for S1, S2, and S3, which have ratios of 1.0 to 3.5.

The freestanding test specimens were fabricated in a commercial UV-LIGA process. All four designs were fabricated from Ni-Fe (denoted as ‘Alpha’) and Ni-Co (denoted as ‘C’) alloys. The nominal layer thickness was 190  $\mu\text{m}$  thick for the Alpha specimens and 170  $\mu\text{m}$  for the C specimens. Twenty-four specimens of each material were tested. Tables 1 and 2 summarize the average dimensions and the standard deviations

**Table 1.** Gauge dimensions for the Alpha specimens. On average, there were six specimens for each design, three tested at a strain rate of 0.001/s and three tested at a strain rate of 1/s. The gauge lengths represented here were the designed values. The thicknesses were measured at the grip sections, and the widths were measured at the gauge sections. The ranges represent the standard deviations.

Specimen design	Nominal gauge length (mm)	Specimen thickness ( $\mu\text{m}$ )	Gauge width ( $\mu\text{m}$ )
S1	2	$189.2 \pm 0.8$	$197 \pm 1.9$
S2	3	$188.8 \pm 1.0$	$498 \pm 1.5$
S3	3	$189.5 \pm 1.2$	$696 \pm 2.4$
S4	1.2	$190.0 \pm 1.1$	$70 \pm 2.3$

**Table 2.** Gauge dimensions for the C specimens. On average, there were six specimens for each design, three tested at a strain rate of 0.001/s and three tested at a strain rate of 1/s. The gauge lengths represented here were the designed values. The thicknesses were measured at the grip sections, and the widths were measured at the gauge sections. The ranges represent the standard deviations.

Specimen design	Nominal gauge length (mm)	Specimen thickness ( $\mu\text{m}$ )	Gauge width ( $\mu\text{m}$ )
S1	2	$171.6 \pm 2.1$	$206 \pm 2.6$
S2	3	$172.6 \pm 2.3$	$508 \pm 2.5$
S3	3	$171.2 \pm 2.8$	$706 \pm 2.1$
S4	1.2	$171.3 \pm 2.8$	$82.3 \pm 1.0$

**Table 3.** Alloy composition ratios (in relative atomic percent) for the Alpha and C specimens.

Specimen design	Alpha specimens (atomic %)	C specimens (atomic %)
S1	93.2 (Ni), 6.8 (Fe)	95.6 (Ni), 4.4 (Co)
S2	88.7 (Ni), 11.3 (Fe)	92.1 (Ni), 7.9 (Co)
S3	90.7 (Ni), 9.3 (Fe)	90.7 (Ni), 9.3 (Co)
S4	95.1 (Ni), 4.9 (Fe)	94.9 (Ni), 5.1 (Co)

in the gauge widths and thicknesses for the as-fabricated specimens. The thicknesses were measured with a digital micrometer at the grip sections. The widths were measured using an optical microscope with a  $5 \times$  objective that had a calibrated conversion factor of  $0.67 \mu\text{m}/\text{pixel}$ . As shown by the data, the fabrication process exhibited tight dimensional control, with  $\leq 1\%$  standard deviation in the gauge section dimensions.

The composition of each alloy and specimen design was determined by EDS in an SEM operated at 30 kV, as shown in table 3. It is important to note that EDS does not give a full composition, mostly due to its sensitivity ranges and limited sensitivities to lighter elements. Here it is used to compare ratios of the primary metallic components. As shown in table 3, both alloys are predominantly nickel-based and show a geometry dependence. In general, the wider the gauge section, the higher the concentration of the secondary element.

The microstructure of each alloy was determined using FIB imaging. The FIB was operated at 30 kV with an aperture producing a 120 pA beam current. As shown in figure 2, the Alpha alloy was an isotropically nanogained material with a grain size of  $\approx 15 \text{ nm}$ , whereas the C alloy was a columnar-grained

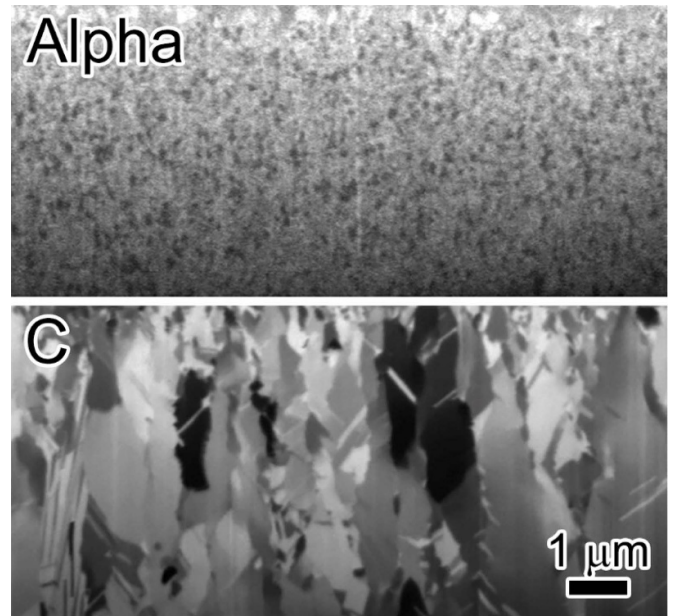


**Figure 2.** FIB micrographs of microstructure for the (a) Alpha and (b) C specimens. The Alpha alloy was an isotropically-nanogained material with a grain size of  $\approx 15 \text{ nm}$ , whereas the C alloy was a columnar-grained material with a grain size of  $\approx 300 \text{ nm}$ .

material with a growth direction perpendicular to the sample face and grain size on the order of 300 nm.

## 2.2. Specimen surface preparation

The as-fabricated LIGA specimens possessed a smooth and highly polished surface. However, to facilitate strain measurements by DIC, we photolithographically fabricated a layer of thin film dots on the specimen top surface to act as fiducial markers, as shown in Figure 3. The dots were two orders of magnitude thinner than the specimen thickness to minimize the impact on the observed mechanical properties. The fiducial markers – each around  $1.5 \mu\text{m}$  thick and  $25 \mu\text{m}$  wide as measured by profilometry – covered the entire gauge section and part of the grip sections of each specimen, were designed with a random orientation and distribution and were found to produce reliable contrast for DIC along the whole gauge sections. It is important to note that even though this method is capable of two-dimensional surface strain mapping over the entire gauge section, in this paper it is only utilized on two ends of the gauge section to measure engineering strain. The 2D surface strain distribution showed uniform deformation until necking.

## 2.3. Tensile testing apparatuses

Tensile tests at the quasi-static strain rate (0.001/s) were conducted by use of a commercial miniature tensile testing stage—originally intended for *in-situ* testing in an SEM—with custom clevises that was mounted under an optical microscope, shown in figure 4. The direction and speed of the motor-driven stage were manually controlled while a

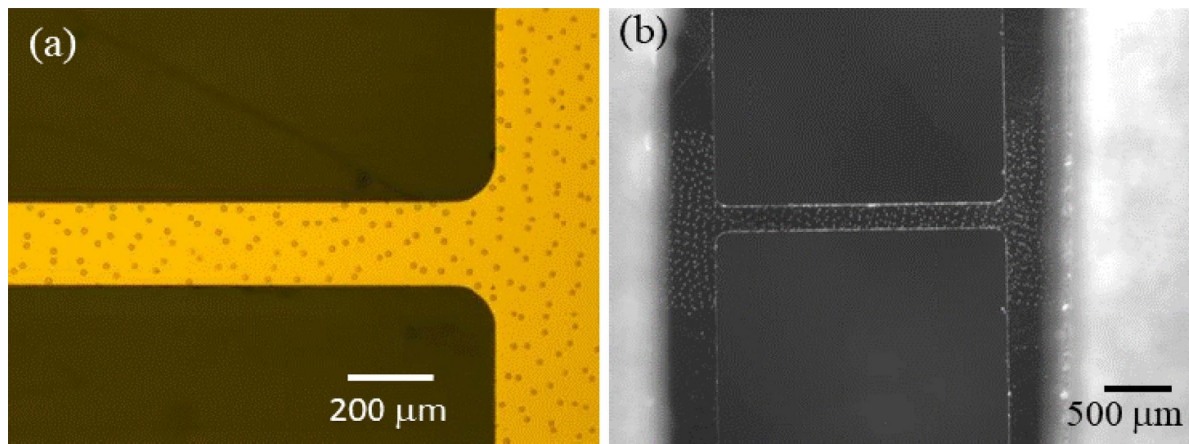


**Figure 3.** (a) Optical micrograph of the top surface of an Alpha specimen (S1 geometry), showing the microfabricated gold dots used as DIC fiducial markers. Specimen widths were measured from similar micrographs. (b) Optical micrograph of the same specimen from (a) during a tensile test at a strain rate of 0.001/s.

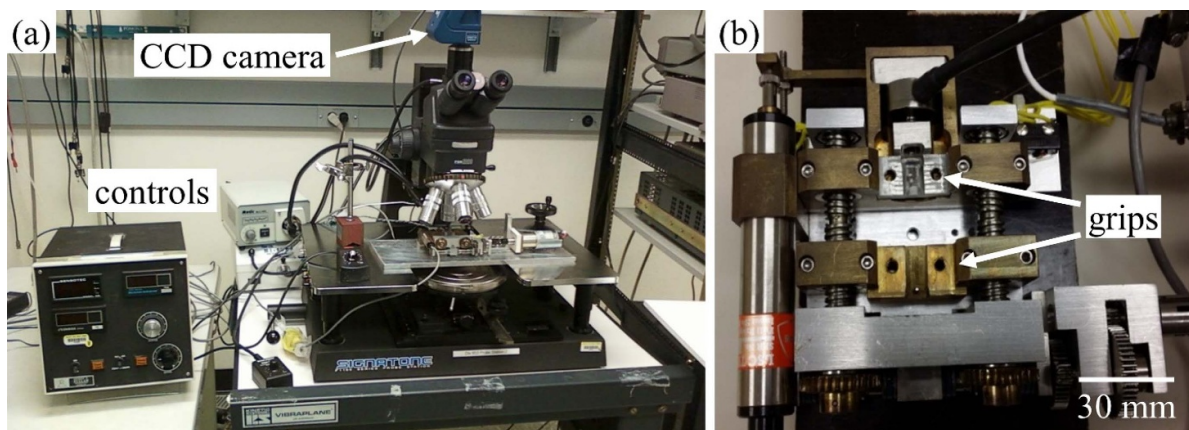


**Figure 4.** (a) Photograph of the tensile test apparatus for the 0.001/s strain rate tests. (b) Close-up photograph of the miniature tensile test stage, which is placed under the microscope in (a).

charge-coupled device (CCD) camera attached to the microscope captured images during the tests. To minimize unintended stresses to the gauge sections during the specimen loading process, the specimens were designed to be pin loaded rather than gripped. Pin loading, while not commonly used for thin-film microscale specimens, is possible in the mesoscale specimens here because of the larger size. Pin loading is also consistent with the ASTM E-8 standard [19] and has the added benefit of specimen self-alignment along the direction of the applied uniaxial load. The forces required to break the specimens ranged from 5 N for the smallest (S4) specimens of the C material to 250 N for the largest (S3) specimens of the Alpha material. A load cell with a maximum force capacity of 334 N (75 lb) was calibrated and installed to accommodate all specimens. From the calibration curves, the absolute force uncertainty of the load cell was found to be 0.5 N, which was more than sufficient for achieving a targeted  $\leq 15\%$  uncertainty in ultimate tensile strength for the smallest (S4) specimens. For most tests, a pre-load of  $\approx 10\%$  of the maximum force was applied to straighten the specimen in the clevises and allow the specimen to shift into place before the start of the test. Specimen shifting at the start of a tensile test is common, both at the

macroscale [20, 21] and micro- and mesoscales [22]. During tests, the CCD camera captured images of the gauge section at a frame rate of 1 image  $s^{-1}$  at an image resolution of 3072 pixels  $\times$  2300 pixels, which corresponds to a spatial resolution of about 1.4  $\mu m$ /pixel, while a custom data acquisition program converted load cell voltage to force at a sampling rate of 200 averaged over 1 s. Following fracture, the force data and images were analyzed offline to construct the engineering stress–strain curves.

The miniature tensile testing stage used for the 0.001/s tests could not reach the loading speeds required to achieve strain rates of 1/s, so, for these higher rate tests, a commercial tabletop servo-hydraulic universal load frame was used, as shown in figure 5. This machine is designed for a wide range of force values; a 5 kN load cell was used here, as it was the smallest available. The load cell was calibrated by the manufacturer and reported to be accurate to 1% of the reading, and from our calibrations we calculated a force uncertainty of about 3% for the lowest forces of 1–20 N which were seen by the smallest (S4) specimens. Custom clevises similar to those installed in the static test apparatus were designed to couple the pin-loaded mesoscale specimens to the much-larger hydraulically

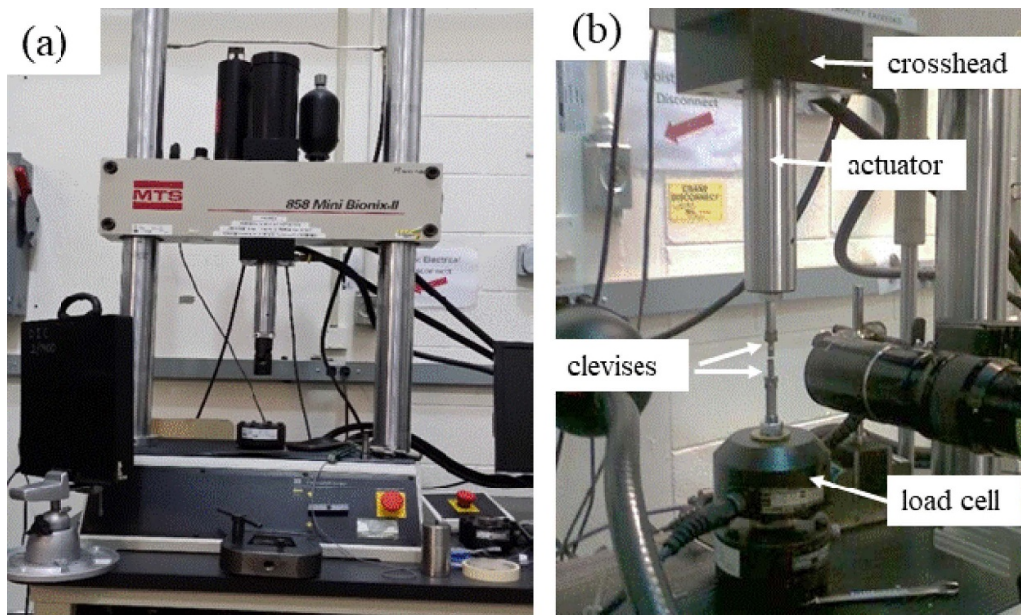


**Figure 5.** (a) Photograph of the tensile test apparatus for the 1/s strain rate tests. (b) Close-up photograph of the load train, clevises, and high-speed camera.

driven actuator, as shown in figure 5(b). Images during the tests were captured with a high-speed camera. A long-distance microscope system was augmented with a  $3 \times$  objective lens, which provided a field of view of approximately 2 mm square in the camera. This allowed capture of the 2 mm-long gauge section of the specimens at the full image resolution of the camera, which was 600 pixels  $\times$  800 pixels and which corresponded to a spatial resolution of about  $10 \mu\text{m}/\text{pixel}$ . The frame rate for the camera was set to 1500 frames/s or one image every 0.67 ms. Also, unlike the static-test apparatus, the camera and load frame here were controlled by separate computers, connected by an electronic trigger, thus the post-test analysis required an additional step of inspecting the images and force data and using the time of specimen fracture to synchronize the forces and images to each other.

#### 2.4. Digital image correlation

A custom DIC program was written for analyzing the tensile tests. The output was a spreadsheet of raw displacements, which were then analyzed to calculate strains. The accuracy of the DIC methods was validated on the present mesoscale specimens down to a strain of 0.001 by comparing the strains we obtained from our DIC program with an image-processing software [23] generated simulated strain, as well as the strain measured with a commercial DIC software. Our strain resolution was 0.0001, and the uncertainty in the strain varied with the strain value (being lower for larger strains) and the specimen size (being higher for smaller specimens). At a strain of 0.001, the relative uncertainty in the strain ranged from 9% for the largest (S3) specimen geometry, to 16% for the smallest (S4) geometry.

It is important to note that several studies [7–9, 11, 16, 17] have used laser-based strain measurement techniques to

conduct tensile testing of similarly-sized LIGA specimens, thus potentially allowing for more accurate measurements of engineering strains below 0.001. Such approaches, however, can only measure strain between pre-determined marks or features on the specimen and may not be suitable for dynamic tests, whereas DIC allows for local as well as full-field strain measurements, strain mapping, as well as measurement of strain uniformity and crack propagation. Recently, DIC of optical micrographs was used for tensile testing of single-crystal silicon specimens with gauge dimensions in the tens of  $\mu\text{m}$  [24],  $25 \mu\text{m}$  and  $35 \mu\text{m}$ -thick films of nanocrystalline and microcrystalline electrodeposited Ni [15], as well as  $10 \mu\text{m}$ -thick nanograined Ni-Fe with a 2 mm-long gauge section [25], but, in these studies, the DIC was performed on a section of the gauge lengths rather than over the entire gauge lengths. In the present work, our technique of patterning microengineered fiducial markers on the specimens enabled 2D surface strain distribution to be reliably obtained over the entire gauge sections of the specimens. As these strain maps were not critical to the analysis presented in this paper, details of this technique and strain distributions obtained will be presented elsewhere.

#### 2.5. Strain hardening analysis

The strain hardening exponent  $n$  and the strength coefficient  $A$  were obtained by fitting the tensile data in the region between the 0.002 offset yield and ultimate tensile strength to the Hollomon equation [26]:

$$\sigma_t = A\varepsilon_p^n \quad (1)$$

where  $\sigma_t$  is the true stress and  $\varepsilon_p$  is the true plastic strain. Since the surface strain distributions from DIC showed uniform deformation until necking, and only the stress and strain

values between yield and ultimate tensile strength before the onset of necking were fitted, the true stress was found from:

$$\sigma_t = \sigma (1 + \varepsilon) \quad (2)$$

where  $\sigma$  is the engineering stress and  $\varepsilon$  is the engineering strain. The true total strain was also found by

$$\varepsilon_t = \ln(1 + \varepsilon). \quad (3)$$

The plastic strain  $\varepsilon_p$  was then calculated by subtracting the elastic strain via Hooke's Law from  $\varepsilon_t$  in equation (3).  $n$  and  $A$  were found by plotting  $\log(\sigma_t)$  vs.  $\log(\varepsilon_p)$ . If the data plotted in this manner is a straight line, the slope is  $n$  and the intercept with the vertical axis is  $\log(A)$ .

Several variations of this basic power law equation may also be used. For example, for LIGA Ni, Williams [27] used the Tomkins equation [28], which appears to be identical to the Hollomon equation, to fit the data of previous work [11, 16, 29]. In contrast, Namazu and Inoue [30] fit their data to the Ludwik equation [31] as given by

$$(\sigma_t - \sigma_Y) = A\varepsilon_p^n \quad (4)$$

where  $\sigma_Y$  is the 0.002 offset yield stress. Comparing the analysis using equations (1) and (4) reveals two important points: First, equation (1) better approximated our data, as evidenced by the larger  $R^2$  values from the linear least squares fit to the  $\log(\sigma_t)$  vs.  $\log(\varepsilon_p)$  data, and, second, there can be up to  $4 \times$  differences in the extracted values for  $n$  and  $A$  depending on the equation. As such, equation (1) was used to extract  $n$  and  $A$  for all specimens in this study.

## 2.6. Fractography and true strain to failure analysis

The fractured surfaces of failed specimens were examined in an SEM operated at 30 kV to determine the final specimen cross-section and the fracture mode. Final strains to failure were calculated by comparing the final specimen cross-section to the initial sample dimensions, measured optically. Top-down plan-view imaging of the fracture surface was found to be the most reliable method, due to plastic deformation of the sample, but results were comparable to those found by measuring sample widths and thickness after failure and comparing to initial measurements. Plan-view imaging allowed variations in roughness contributing to fracture surface area, but not to cross-sectional area, to be ignored. However, three-dimensional information is needed to ensure that the correct area is selected. This three-dimensional information was acquired by taking stereo-pairs at  $0^\circ$  and  $8^\circ$  sample tilt and combining the images into a red-blue three-dimensional stereogram. Using the information from the three-dimensional stereogram, the cross-sectional area was colored in on the plan-view image, and the area measured by image-processing software. This area in pixels was converted to  $\mu\text{m}^2$  and corrected for instrument error (6% to 9% for our SEM, depending on magnification). Reduction in area  $RA$  was calculated by

$$RA = \frac{(A_i - A_f)}{A_i} \quad (5)$$

where  $A_i$  is the initial cross-sectional area, and  $A_f$  is the final cross-sectional area, as measured above. The true strain at failure  $\varepsilon_f$  was also calculated via

$$\varepsilon_f = -\ln\left(\frac{A_f}{A_i}\right). \quad (6)$$

## 2.7. Error analysis

Relative uncertainties were calculated for each property for each material/geometry/rate reported in the following sections. In an accompanying publication, we will discuss the details of these error analyses, as well as the contributions of various experimental factors to the uncertainties, comparisons between the uncertainties and the standard deviations in the properties across all the material/size/rate categories, and the resulting implications for applying these properties to MEMS engineering and design. A brief summary of the primary sources of uncertainties presented in this paper is provided here.

The relative uncertainty in the ultimate tensile strength was calculated by first determining the absolute uncertainties in the forces and specimen cross sectional areas and adding them in quadrature: the absolute uncertainty in the force was determined from calibrating the loadcell, and the relative uncertainty in the specimen cross sectional area was determined from the uncertainty in the thickness as measured by a digital micrometer, and the uncertainty in the gauge width (the difference in width when measured from the top versus the bottom surfaces), assuming a rectangular cross section. The relative uncertainty in the apparent Young's modulus was determined from calculating the relative uncertainties in the stresses and strains at a nominal strain value of 0.001; the relative uncertainty in stress was determined in a manner similar to the uncertainty in the ultimate tensile strength, while the relative uncertainty in the strain was calculated from the relative uncertainties in the gauge length and displacement as measured by DIC. The absolute uncertainty in our DIC methods was taken as 0.2 pixels which corresponds to  $0.28 \mu\text{m}$  for the specimens tested at 0.001/s. The relative uncertainty in the 0.2% offset yield strength was initially calculated based on a procedure developed by Matusevich *et al* for macroscale tensile tests [32], but since the relative uncertainty in the apparent Young's modulus was found to be large (exceeding 30%) in several of our material/geometry/rate categories, and given that the modulus value affects the determination of the 0.2% yield strength, we then combined the relative uncertainties in modulus with the preliminary relative uncertainty in the yield strength to obtain a final total relative uncertainty in the 0.2% offset yield strength for each specimen category. The uncertainties in the strain hardening exponent and strength coefficient were calculated by using standard statistical methods to calculate the uncertainties in the slopes and intercepts of the log-log plots of the Hollomon equation (equation (1)).

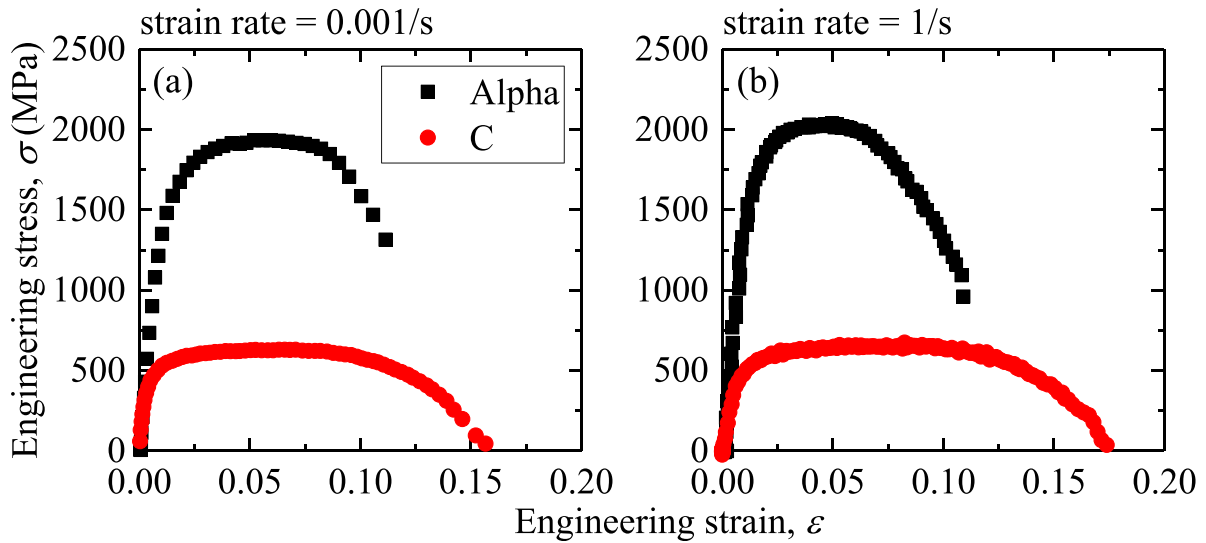


**Figure 6.** Typical engineering stress–strain curves for Alpha and C specimens (S1 geometry), tested at strain rates of (a) 0.001/s and (b) 1/s.

### 3. Results and discussion

Three specimens of each material/geometry/rate combination were tested at room temperature, for a total of 48 specimens. The engineering stress ( $\sigma$ )–strain ( $\epsilon$ ) curves for each specimen can be found in the appendix of [33], and a true stress–strain curve of the Alpha S1 geometry as assessed by finite element analysis can be found in ref. [34]. Figure 6 shows typical engineering  $\sigma$ – $\epsilon$  curves for specimens of the S1 geometry, tested at strain rates of 0.001/s and 1/s. The curves for the S2, S3, and S4 geometries are qualitatively similar. The engineering stress was calculated as the force measured by the loadcell divided by the specimen’s initial cross-sectional area. The engineering strains were measured by use of DIC as described earlier. For all  $\sigma$ – $\epsilon$  curves, the apparent Young’s modulus ( $E$ ), 0.2% offset yield strength ( $\sigma_Y$ ), ultimate tensile strength ( $\sigma_{UTS}$ ), strain hardening exponent ( $n$ ), and strength coefficient ( $A$ ) were determined. The true strains to failure ( $\epsilon_f$ ) were also assessed from fractography.

For  $E$ , most  $\sigma$ – $\epsilon$  curves exhibited a single linear region at small  $\epsilon$ , which allowed  $E$  to be determined simply through the slope of the curve. However, in some cases, the  $\sigma$ – $\epsilon$  curves revealed two distinct linear regions with different slopes: An initial linear region up to strains of approximately 0.0005 to 0.001 (the ‘low-strain region’), followed by a second linear region up to  $\approx 0.01$  (the ‘high-strain region’). Since the specimens were preloaded before the start of the test to enable specimen self-alignment, and no evidence of further self-alignment was observed during the test, the presence of two linear regions is unlikely to be due to specimen shifting. Other researchers have described similar behavior in LIGA Ni specimens of similar dimensions [35], while in order-of-magnitude smaller Ni specimens, the modulus increased due to room temperature creep [15]. For microcrystalline Ni such as the C alloy, one explanation is that the distinct regions were due to changes in the dislocation structures as a function of strain amplitude [36]. For nanocrystalline Ni such as the Alpha alloy, it was

proposed that because the grains are too small to accommodate dislocation networks, the mechanistic origins of such effects might include time-dependent, irreversible grain boundary processes [37]. Despite the different underlying mechanisms, behavior such as these have been categorized under the general umbrella of microplasticity, see for example the review in ref [38]. In the present study, for specimens with two distinct linear regions, the  $E$  reported here were calculated from the high-strain region, given that most structural applications will involve strains greater than 0.0005 and most devices will be subjected to proof testing. However, for completeness,  $E$  values from both regions have been presented in a previous report [33].

For  $\sigma_Y$ , the predetermined value for  $E$  and a 0.2% offset were used to determine the yield strength.  $\sigma_{UTS}$  was taken to be the maximum stress on the  $\sigma$ – $\epsilon$  curves.  $n$  and  $A$  were obtained by fitting the tensile data in the region between  $\sigma_Y$  and  $\sigma_{UTS}$  to equation (1).

While not evident for the four specimens shown in figure 6, for other specimens in this study it appeared that the materials are more ductile at the higher strain rate; however, this is partially an artifact of the different testing apparatuses for each strain rate. The apparently larger strains to failure for some of the 1/s tests in our previous report [33] are partially due to the availability of more strain data (images) at the end of the test due to the use of the high speed camera. Consequently, the true strains at failure ( $\epsilon_f$ ) in this study were determined from fractography per equation (6).

#### 3.1. Elastic modulus, yield strength, and ultimate tensile strength

The apparent Young’s moduli ( $E$ ) for the Alpha and C specimens as a function of gauge width at strain rates of 0.001/s and 1/s are shown in figures 7(a) and (b), respectively. A two-way ANOVA with replication and a significance level of 0.05 (for 95% confidence) was performed on the two alloys.

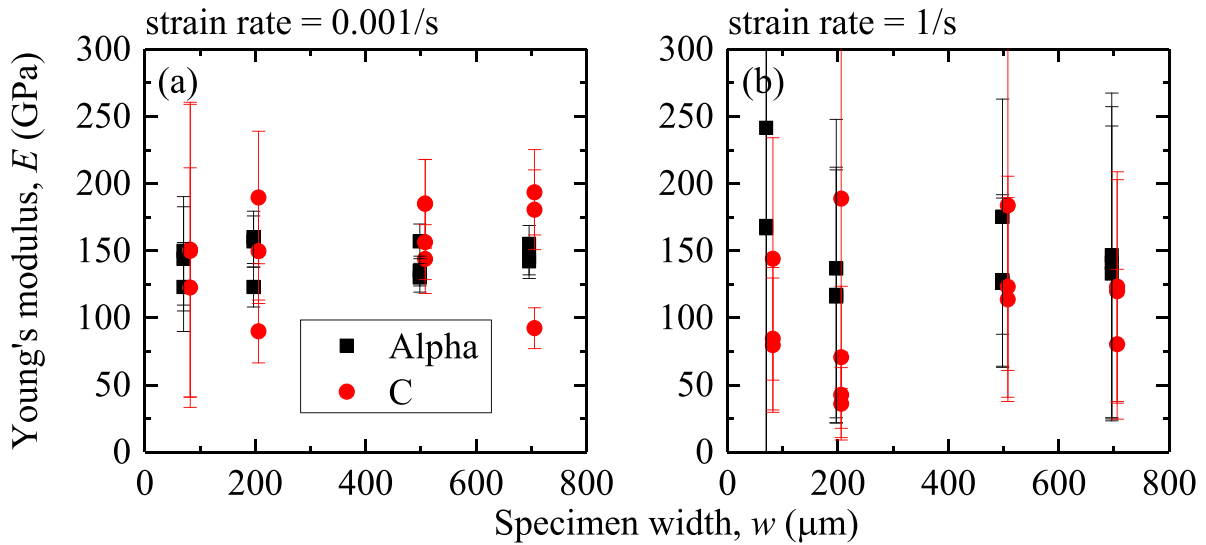


**Figure 7.** Apparent Young's modulus as a function of specimen gauge width for Alpha and C specimens, tested at strain rates of (a) 0.001/s and (b) 1/s. The error bars represent measurement uncertainty, as determined from error analysis.

The ANOVA results showed that  $E$  does not vary with the gauge width. For the Alpha specimens,  $E$  is also independent of strain rate; at 0.001/s, the average value is 143 GPa, whereas at 1/s, the average value is 150 GPa. For the C specimens, the ANOVA also indicated no rate effect on  $E$ ; however, the C data failed one of the assumptions for validity—Levene's test for homogeneity of variances—and thus the conclusion of no rate effect may not be valid. Indeed, for the C specimens the average value of  $E$  decreases significantly with strain rate, with an average value of 153 GPa at 0.001/s and 107 GPa at 1/s. However, a clear determination of such trends is difficult, given the large measurement uncertainties.

It has been well documented in the literature on conventional macroscale mechanical testing that the Young's modulus is the least reliable property obtained from a tensile test and is best obtained from dynamic methods [20, 21]. The reasons for this are exacerbated as the specimen size decreases, while other experimental factors also begin to contribute to the measurement uncertainty. In the present study, the smallest measurement uncertainties for Young's modulus was  $\approx 10\%$  (Alpha S2 and S3 geometries at 0.001/s). The closest comparison in Young's modulus uncertainties from the literature is Banks-Sills *et al* [24], who, even with absolute uncertainty of  $<0.01$  pixels in their DIC (while ours is  $\approx 0.2$  pixels), and on single-crystal silicon (which is perfectly elastic), calculated an error in  $E$  of up to 4%. In all, our measurement uncertainties in  $E$  ranged from 10% to 100% depending on material composition, specimen width, and strain rate. It is our opinion that many of these issues are applicable to contemporary works in the literature on LIGA Ni alloys and may help to shed some light on the wide discrepancies in the reported values for  $E$ .

Despite large measurement uncertainties, it is evident that the average  $E$  we reported above are smaller than those typically cited for both bulk coarse-grained Ni (207 GPa) [39] and other LIGA Ni alloys (158 GPa to 190 GPa) [7, 11, 14, 30, 35]. There are three potential reasons for the reduction in  $E$ : (1)

crystallographic orientation, (2) microstructure and chemistry, and (3) porosity. With respect to (1), Hemker and Last [7] showed that the Reuss [40] and Voigt [41] averages for  $E$  assuming a  $\langle 001 \rangle$  out-of-plane texture and no preferred in-plane orientation were 171 GPa and 177 GPa, respectively, but also that  $E$  reached a minimum value of 136 GPa along the  $\langle 100 \rangle$  directions and 323 GPa along the  $\langle 110 \rangle$  directions. Therefore, a slight in-plane preference in the  $\langle 100 \rangle$  directions would have the potential to decrease the average  $E$  from the Reuss and Voigt averages and typical experimental values. With respect to (2), Mazza *et al* showed that  $E$  for Ni and Ni-Fe microbars were 202 GPa and 119 GPa, suggesting that the inclusion of 50% Fe resulted in almost a  $2 \times$  reduction in elastic modulus [10]. As shown in table 3, the Alpha films tested here exhibited Fe concentrations ranging from 4.9% to 11.3%, implying that the effect is subtler in our case. With respect to (3), Cho *et al* [16] used the porosity model of Krstic *et al* [42] to demonstrate that  $<1\%$  cracked spherical pores would decrease  $E$  from the expected value of 177 GPa to their measured value of 163 GPa. Such pores have not been observed here, but their presence can also not be dismissed. Altogether, these three mechanisms could have contributed to the observed  $E$  here and might also explain similar results in other studies [8]. In addition, Wang *et al* [18] reported a size effect on the Young's modulus of electrodeposited Ni, measured by tensile tests. In the present study, the ANOVA analysis on our data indicated no size effect for either alloy, within the size range of samples. It should be noted that most of these prior studies do not report measurement uncertainties in their  $E$  values, and thus it is difficult to make direct comparisons among studies, given that  $E$  is in general difficult to obtain reliably from tensile tests [20, 21].

Yield strength ( $\sigma_Y$ ) for Alpha and C specimens as a function of gauge width at strain rates of 0.001/s and 1/s are shown in figures 8(a) and (b), respectively. The changes with alloy composition are the most significant;  $\sigma_Y$  varied from 1249 MPa to

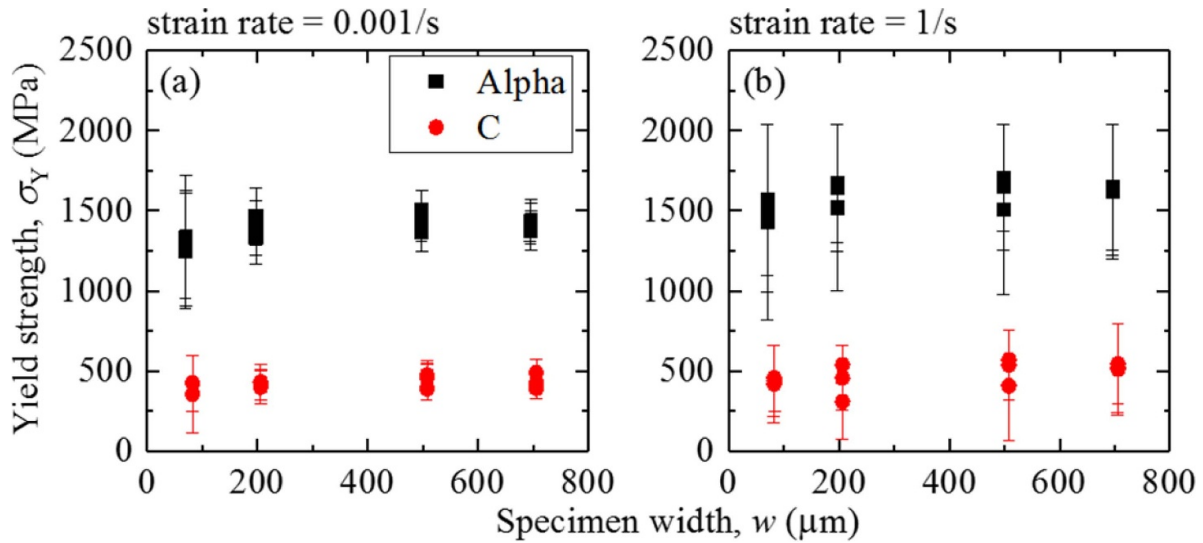


**Figure 8.** Yield strength as a function of specimen width for Alpha and C specimens, tested at strain rates of (a) 0.001/s and (b) 1/s. The error bars represent measurement uncertainty, as determined from an error analysis for each specimen.

1705 MPa for the Alpha specimens and 310 MPa to 571 MPa for the C specimens, pointing to a  $3 \times$  change in  $\sigma_Y$  due to film microstructure and chemistry. For each alloy, a two-way ANOVA with replication was performed to discern size and rate effects. The ANOVA confirmed the presence of rate effects on  $\sigma_Y$  for both the Alpha and C materials, but a size effect only for Alpha. The size effect in Alpha is small, with the larger widths leading to larger  $\sigma_Y$ . The changes in  $\sigma_Y$  with strain rate are more evident; at 0.001/s, the average  $\sigma_Y$  for Alpha and C specimens were 1380 MPa and 425 MPa, whereas at 1/s, the average  $\sigma_Y$  for Alpha and C specimens were 1590 MPa and 475 MPa. Thus,  $\sigma_Y$  increased 10% to 15% with strain rate for both materials. However, as with  $E$ , a definitive assessment of  $\sigma_Y$  trends is limited by large measurement uncertainties.

The magnitude of the uncertainty in the yield strength follows that of the corresponding uncertainty in apparent Young's modulus. Young's modulus determines the point of intersection between the 0.002 offset line and the stress-strain curve, and due to the large uncertainties in  $E$  as discussed earlier, we felt it critical to include these in the  $\sigma_Y$  uncertainty calculations to obtain more conservative values for the upper and lower bounds of  $\sigma_Y$ . The uncertainty in  $E$  thus dominates the uncertainty in  $\sigma_Y$  and exceeds the statistical variation (standard deviation) in all the material composition, specimen width, and strain rate combinations, particularly those for the 1/s tests.

The average extracted  $\sigma_Y$  values for Alpha and C specimens are consistent with literature data on fine-grained Ni-Fe (730 MPa to 1800 MPa) [10–12] and coarse-grained Ni (275 MPa to 441 MPa) [7, 8, 35] thin films. The reported size effect in our Alpha specimens is also in agreement with other studies on LIGA Ni alloys. For instance, Cho *et al* [16] showed that the yield strength decreased from 370 MPa for specimen widths greater than 200  $\mu\text{m}$  to 310 MPa at a specimen width of 50  $\mu\text{m}$ . With respect to the changes in  $\sigma_Y$  with

composition, it has been revealed that the hardness (and thus yield strength) of nanocrystalline Ni increases as grain size decreases, following a Hall–Petch relationship [43]. As such, the increase in  $\sigma_Y$  from C to Alpha specimens can be attributed to a decrease in the average grain size from  $\approx 300$  nm to 15 nm as shown in figure 2. Previous work [43, 44] has suggested that the Hall–Petch relation for nanocrystalline Ni breaks down at a critical grain size between 10 nm and 15 nm, which suggests that deformation in the Alpha specimens likely takes place via creep-like processes as opposed to dislocation processes. The rate-dependence observed in the Alpha and C specimens is in accordance with Schwaiger *et al* [14].

Ultimate tensile strengths (UTSs) for Alpha and C specimens as a function of specimen width at strain rates of 0.001/s and 1/s are shown in figures 9(a) and (b), respectively. The trends for UTS are similar to those for yield strength:  $\sigma_{UTS}$  exhibited a slight size effect (larger widths leading to larger  $\sigma_{UTS}$ ), and moderate strain-rate effect (larger strain rates leading to larger  $\sigma_{UTS}$ ), as supported by two-way ANOVA performed on each alloy. The ANOVA result indicated no interaction between size and rate, however. And as with the yield strength, smaller grain size leads to higher  $\sigma_{UTS}$ . Altogether, the average  $\sigma_{UTS}$  for Alpha and C specimens at 0.001/s were 1915 MPa and 653 MPa, whereas at 1/s they were 2041 MPa and 712 MPa, pointing to a 6% to 9% increase with strain rate and a  $3 \times$  change with microstructure and chemistry. The measurement uncertainty in the UTS was  $<2\%$  for all specimens except the smallest S4 specimens, for which it was up to 12%. The largest contribution to the uncertainty in the UTS was the uncertainty in gauge width caused by the slightly sloped specimen sidewalls. As with the  $\sigma_Y$  results, the  $\sigma_{UTS}$  for Alpha and C specimens are similar to the work on films of fine-grained Ni-Fe (1625 MPa to 2400 MPa) [10–12] and coarse-grained Ni (460 MPa to 758 MPa) [7, 8, 35]. The  $\sigma_Y/\sigma_{UTS}$  ratios here are also in agreement with those from the aforesaid studies ( $\approx 0.6$  to 0.8). The underlying mechanisms responsible

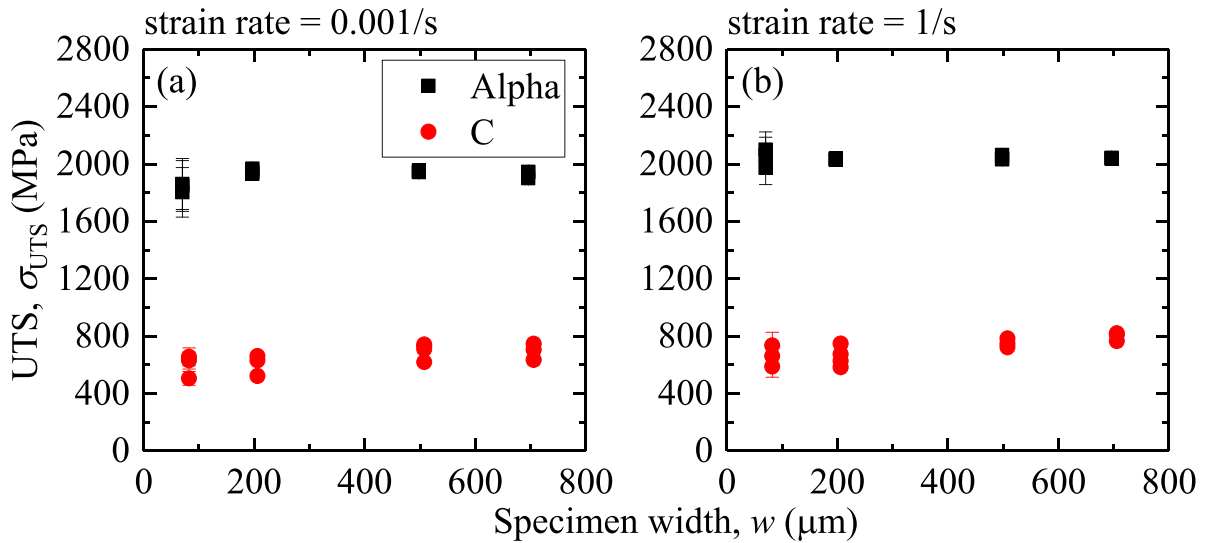


**Figure 9.** UTS as a function of specimen width for Alpha and C specimens, tested at strain rates of (a) 0.001/s and (b) 1/s. The error bars represent measurement uncertainty, as determined from error analysis.

for these trends are similar to those listed above for  $\sigma_Y$ , with the lone exception the suggestion that the size effect for  $\sigma_{UTS}$  may be due to the influence of the specimen geometry on the onset of necking and not fundamental changes in the material properties [16].

### 3.2. Strain hardening exponent and strength coefficient

It should be noted that in the literature on LIGA Ni alloys, strain hardening has so far been given less attention than other mechanical properties. Strain hardening exponents ( $n$ ) and strength coefficients ( $A$ ) for the Alpha and C specimens as a function of specimen gauge width at strain rates of 0.001/s and 1/s are shown in figures 10(a) and (b), respectively. A two-way ANOVA with replication was performed on the  $n$  and  $A$  of each alloy separately, to determine the presence of size and rate effects. For the Alpha specimens, it was found that neither size nor rate affected the  $n$  and  $A$ , but the data for  $A$  failed Levene's test for homogeneity of variances and thus the dependence (or lack thereof) of  $A$  on size and rate may be inconclusive. For the C specimens, both size and rate effects are present in  $n$ , with  $n$  increasing with both the gauge width and strain rate, and furthermore there is interaction between size and rate. For C there is also a small size effect on  $A$ , with  $A$  increasing slightly with specimen width at both strain rates (similar to the UTS trends in figure 9).

The average value for  $n$  ( $\approx 0.12$ ) is invariant with material composition. In contrast,  $A$  is significantly larger in the Alpha specimens (3033 MPa) than in the C specimens (1070 MPa), which is expected given the larger UTS. The standard deviations exceeded the measurement uncertainties, suggesting that the total uncertainty in strain hardening parameters is dominated by specimen-to-specimen variability and not measurement uncertainty.

In a previous study, Williams [27] calculated  $n$  and  $A$  for LIGA-fabricated Ni and Ni-20%Fe specimens based on the data from Sharpe and McAleavey [11], Cho *et al* [16], and

Christenson *et al* [29]. The extracted  $n$  ranged from 0.12 to 0.19 for the Ni specimens and 0.1 to 0.8 for the Ni-Fe specimens, while Lou *et al* [17] also reported  $n$  of 0.11 for 100  $\mu\text{m}$ -thick LIGA Ni. These previous studies are in good agreement with the results for C and Alpha in figure 10 (our  $n$  being at the lower end of the comparison range). In contrast, the  $A$  extracted by Williams was significantly smaller than those here;  $A$  ranged from 383 MPa to 475 MPa for Ni and 1186 MPa to 2165 MPa for Ni-Fe. The significant disparity in  $A$  is likely due to the Hall–Petch effect; previous work was mainly based on materials with  $\mu\text{m}$ -sized grains, whereas the current study is based on materials with nm-sized grains, as shown in figure 2.

In contrast, Namazu and Inoue [30] reported values of  $n$  and  $A$  that were significantly larger than those here and in Williams [27] and Lou *et al* [17]. At room temperature, their  $n$  was  $0.71 \pm 0.1$  and  $A$  was  $4.55 \pm 1.8$  GPa, with the uncertainties being the standard deviations. One possibility is related to differences in specimen geometry; the film thickness in Namazu and Inoue was 10  $\mu\text{m}$ , which is more than an order of magnitude thinner than the specimens examined here and by others [17, 27] and could result in size effects. Another possibility is related to the choice of the power-law equation fit to the  $\sigma$ - $\epsilon$  data. As noted earlier, the data here and in Williams [27] and Lou *et al* [17] were analyzed with equation (1), whereas the data in Namazu and Inoue [30] were analyzed with equation (4). From fitting our data to both equations, we found our  $n$  and  $A$  to increase by as much as  $4 \times$  and  $1.5 \times$ , respectively, when using equation (4). We finally chose equation (1), as it better approximated the present data and allowed for more comparisons to the literature.

### 3.3. Fractography and true strain to failure

The fracture surfaces of failed Alpha and C specimens were examined as shown in figure 11. The fracture surfaces on the Alpha alloy largely followed the same pattern: macroscopically flat and perpendicular to tensile axis 'brittle' fracture

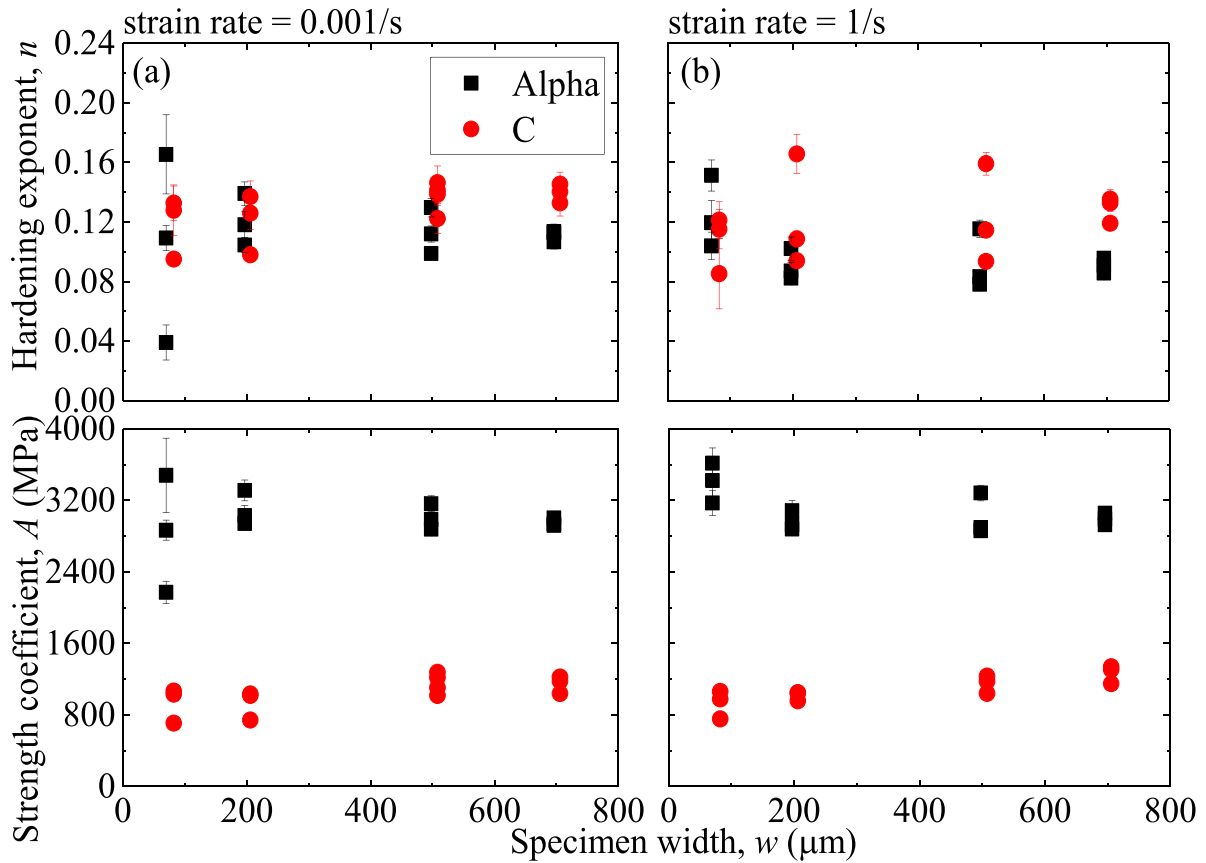


**Figure 10.** Strain hardening exponent and strength coefficient as a function of specimen width for Alpha and C specimens, tested at strain rates of (a) 0.001/s and (b) 1/s. The error bars represent measurement uncertainty, as determined from an error analysis for each specimen.

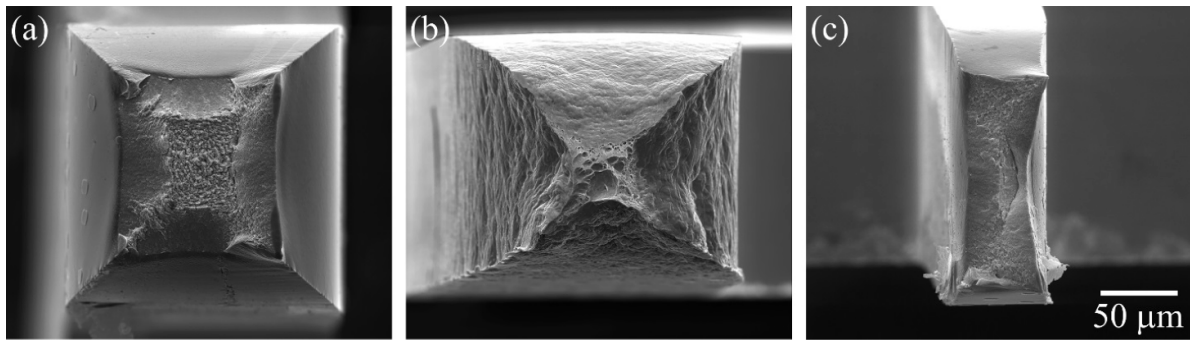


**Figure 11.** Fracture surfaces for (a) Alpha and (b) C specimens (S1 geometry). The Alpha specimen shows significantly less reduction in area than the C specimen. (c) Fracture surface for an Alpha specimen (S4 geometry). In this case, the surface is dominated by smoother fracture features, in contrast to the Alpha surface in (a).

centered in a cup-cone final failure. An exception to this cup-cone failure was found in the S4 geometries; the majority failed at a 45° shear angle, which was quite smooth in texture, though, in some cases, a small percentage of the fracture surface was still covered by flat ‘brittle’ fracture perpendicular to the tensile axis. The fracture surfaces on the C alloy can be grouped into two categories: microvoids and knife-edge failures. Microvoids were observed in the S1, S2, and S3 geometries. Samples exhibited clear necking, followed by failure across the remaining area by microvoid coalescence. Knife-edge failures were detected in the S1, S3, and S4 geometries.

More detailed discussions on the fracture mechanism in these specimens can be found elsewhere [45].

True strains to failure ( $\epsilon_f$ ) as obtained from the reduction of area for the Alpha and C specimens as a function of specimen width at strain rates of 0.001/s and 1/s are shown in figures 12(a) and (b), respectively. The clearest trend is the difference in behavior of the two alloys. The Alpha specimens show significantly less ductility than the C specimens, with  $\epsilon_f$  typically around 50% of the value reached by the C specimens. The decrease in  $\epsilon_f$  is independent of strain rate. This difference in behavior is evident when comparing the fracture

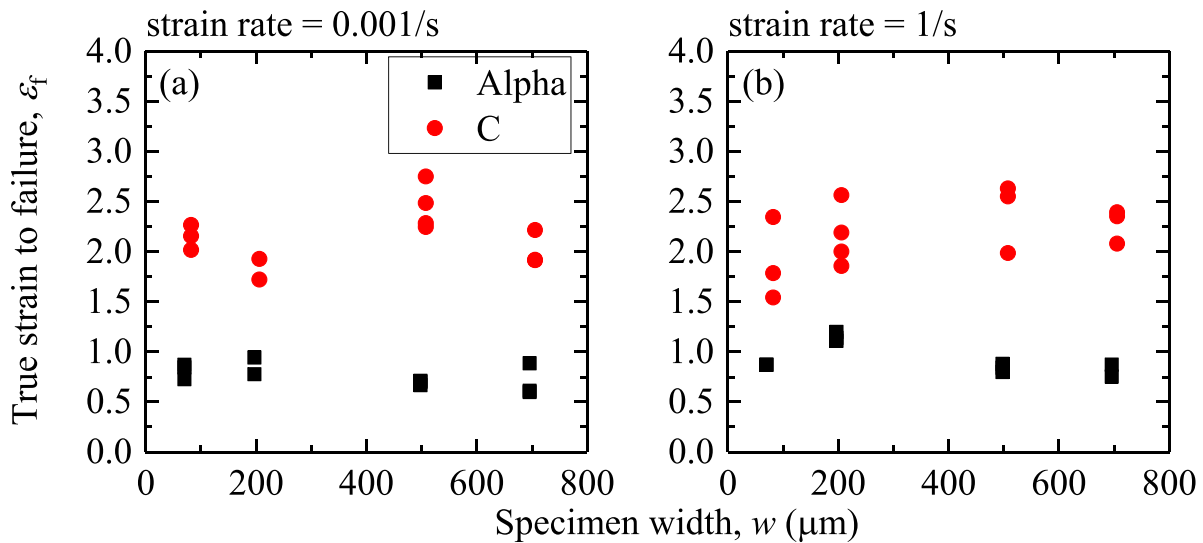


**Figure 12.** True strain to failure, measured via fractography, as a function of specimen width for Alpha and C specimens, tested at strain rates of (a) 0.001/s and (b) 1/s.

surfaces in figures 11(a) and (b). The Alpha specimens also showed significantly less variability in  $\varepsilon_f$  than the C specimens, with statistical variations often half of those observed for the C specimens. With regards to strain rate effects, Alpha specimens exhibited a clear increase in  $\varepsilon_f$  with increased strain rate, with the largest effect observed in the S1 (square) geometry and the smallest observed in the S4 (smallest) geometry. The C specimens showed less of a clear trend, with some geometries showing an increase in  $\varepsilon_f$  with increasing strain rate and others a decrease. These variabilities were often within the statistical variability of the data, suggesting that strain rate is not a critical factor at this degree of ductility.

$\varepsilon_f$  was also influenced by the gauge geometry. For the C specimens, there is a clear increase in  $\varepsilon_f$  in the elongated cross-section geometries (S2, S3, and S4), compared to the square cross-section samples (S1). For the Alpha specimens, the opposite tendency occurred, with the elongated geometries (S2 and S3) showing significantly lower strains to failure than the square geometry (S1). The exception to the trend is the S4 geometry, which at the lower strain rate, showed similar  $\varepsilon_f$  as the S1 geometry. A likely reason for this can be seen by observing the fracture surface in figure 11(c). The small size of the S4 geometry may be unable to support the fracture mechanism observed in the other samples, and this shift in fracture mode may explain the difference in mechanical response. More comprehensive information on the dominant factors for fracture in these alloys can be found elsewhere [45].

#### 4. Conclusions

In summary, we investigated the elastic-plastic properties of 200  $\mu\text{m}$  thick tensile specimens fabricated from a nanograined Ni-Fe ('Alpha') alloy and a micrograined Ni-Co ('C') alloy in a commercial LIGA process with gauge widths ranging from 75  $\mu\text{m}$  to 700  $\mu\text{m}$ . Tensile tests were conducted on 48 specimens at strain rates of 0.001/s and 1/s, where the engineering strains were measured by DIC of thin-film gold

dots fabricated on the specimen surfaces, and true strain to failure was measured via fractography. For each alloy, two-factor ANOVA with replication, at a 95% confidence level, was performed on each property from the tensile test to identify size and rate effects. The apparent Young's modulus, 0.2% offset yield strength, ultimate tensile strength, strain hardening exponent and strength coefficient, and true strain to fracture were reported for each combination of specimen gauge size, strain rate, and material composition. The values for  $E$  were found to be invariant with size, rate, and composition within the measurement uncertainty and were lower than handbook values for bulk material of similar composition, whereas the UTS varied with size, rate and composition. The values for  $\sigma_Y$  and  $\varepsilon_f$  were dependent to varying levels on all three variables. The average value of the strain hardening exponent was similar for both Alpha and C alloys, but the strength coefficient was much higher for Alpha. The  $n$  and  $A$  were independent of gauge size and strain rate for the Alpha alloy, but for the C alloy  $n$  was dependent on both while  $A$  depended only on size. When the smallest specimens were excluded, the results showed measurement uncertainties <10% for the ultimate tensile strength, strain hardening exponent, and strength coefficient, which were less than or equal to the standard deviations of those properties. For the apparent Young's modulus, however, there were several test conditions where the measurement uncertainty was >30%. In fact, for some combinations of material, size, and rate, the measurement uncertainties in  $E$  and  $\sigma_Y$  far exceeded their respective standard deviations, likely stemming from common experimental factors and material microplasticity.

#### Acknowledgments

The authors thank Timothy 'Dash' Weeks at NIST for assistance with calibrating the load cell in the 1/s test set up. Specific commercial equipment, instruments, and materials that are identified in this report are listed in order to adequately

describe the experimental procedure and are not intended to imply endorsement or recommendation by the National Institute of Standards and Technology (NIST). This project was funded by the US Army Combat Capabilities Development Command Armaments Center (CCDC AC) and the Joint Fuze Technology Program (JFTP). The JFTP project number was 14-G-006, Micro Scale Materials and Energetic Effects Characterization.

## ORCID iDs

Li-Anne Liew  <https://orcid.org/0000-0003-0202-026X>  
 David T Read  <https://orcid.org/0000-0003-1479-1619>  
 May L Martin  <https://orcid.org/0000-0002-5153-9597>  
 Frank W DelRio  <https://orcid.org/0000-0003-1727-8220>

## References

- [1] Becker E W, Ehrfeld W, Hagmann P, Maner A and Munchmeyer D 1986 Fabrication of microstructures with high aspect ratios and great structural heights by synchrotron radiation lithography, galvanofarming, and plastic moulding (LIGA Process) *Microelectron. Eng.* **4** 35–6
- [2] Ehrfeld W *et al* 1987 Fabrication of microstructures using the LIGA process *Proc. IEEE Micro Robots and Teleoperators Workshop Hyannis, MA* pp 1–11
- [3] Guckel H, Christenson T R, Skrobis K J, Denton D D, Choi B, Lovell E G, Lee J W, Bajikar S S and Chapman T W 1990 Deep x-ray and UV lithographies for micromechanics *Proc. IEEE Solid-State Sensor and Actuator Workshop Hilton Head Island, SC* pp 118–22
- [4] Christenson T R and Guckel H 1995 Deep x-ray lithography for micromechanics *Proc. SPIE* **2639** 134–45
- [5] Safranek W H 1986 *The Properties of Electrodeposited Metals and Alloys: A Handbook* (Orlando, FL: American Electroplaters Society)
- [6] Dini J W 1993 *Electrodeposition: The Materials Science of Coatings and Substrates* (Park Ridge, NJ: Noyes Publications)
- [7] Hemker K J and Last H 2001 Microsample tensile testing of LIGA nickel for MEMS applications *Mater. Sci. Eng. A* **319–21** 882–6
- [8] Buchheit T E, LaVan D A, Michael J R, Christenson T R and Leith S D 2002 Microstructural and mechanical properties investigation of electrodeposited and annealed LIGA nickel structures *Metall. Mater. Trans. A* **33** 539–54
- [9] Tang J, Wang H, Guo X Q, Liu R, Dai X H, Ding G F and Yang C S 2010 An investigation of microstructure and mechanical properties of UV LIGA nickel thin films electroplated in different electrolytes *J. Micromech. Microeng.* **20** 025033
- [10] Mazza E, Abel S and Dual J 1996 Experimental determination of mechanical properties of Ni and Ni-Fe microbars *Microsyst. Technol.* **2** 197–202
- [11] Sharpe W and McAleavey A 1998 Tensile properties of LIGA nickel *Proc. SPIE* **3512** 130–7
- [12] Li H and Ebrahimi F 2006 Tensile behavior of a nanocrystalline Ni-Fe alloy *Acta Mater.* **54** 2877–87
- [13] Wang N, Wang Z, Aust K T and Erb U 1997 Room temperature creep behavior of nanocrystalline nickel produced by an electrodeposition technique *Mater. Sci. Eng. A* **237** 150–8
- [14] Schwaiger R, Reszat J-T, Bade K, Aktaa J and Kraft O 2009 A combined microtensile testing and nanoindentation study of the mechanical behavior of nanocrystalline LIGA Ni-Fe *Int. J. Mater. Res. (formerly Z. Metallkd.)* **100** 68–75
- [15] Collins J G, Wright M C and Muhlstein C L 2011 Cyclic stabilization of electrodeposited nickel structural films *J. Microelectromech. Syst.* **20** 753–63
- [16] Cho H S, Hemker K J, Lian K, Goettert J and Dirras G 2003 Measured mechanical properties of LIGA Ni structures *Sensors Actuators A* **103** 59–63
- [17] Lou J, Allameh S, Buccheit T and Soboyejo W O 2003 An investigation of the effects of thickness on mechanical properties of LIGA nickel MEMS structures *J. Mater. Sci.* **38** 4129–35
- [18] Wang H, Liu R, Mao S-P, Tang J, Zhang -C-C and Ding G-F 2009 Effect of specimen size on Young's modulus of electrodeposited Ni *Surf. Rev. Lett.* **16** 303–7
- [19] ASTM Committee E8 2013 *Standard test methods for tension testing of metallic materials (ASTM E8/E8M)* (West Conshohocken, PA: ASTM)
- [20] Lord J D and Morrell R 2006 *Measurement Good Practice Guide No 98: Elastic Modulus Measurement* (London: National Physical Laboratory)
- [21] Lord J D and Morrell R 2010 Elastic modulus measurement – obtaining reliable data from the tensile test *Metrologia* **47** S41–9
- [22] Sharpe W N, Bagdahn J, Jackson K and Coles G 2003 Tensile testing of MEMS materials – recent progress *J. Mater. Sci.* **38** 4075–9
- [23] Abramoff M D, Magalhaes P J and Ram S J 2004 Image processing with ImageJ *Biophotonics Int.* **11** 36–42
- [24] Banks-Sills L, Shklovsky J, Krylov S, Bruck H A, Fourman V, Eliasi R and Ashkenazi D 2011 A methodology for accurately measuring mechanical properties on the micro-scale *Strain* **47** 288–300
- [25] Sharon J A, Padilla I I H A and Boyce B L 2013 Interpreting the ductility of nanocrystalline metals *J. Mater. Res.* **28** 1539–52
- [26] Hollomon J H 1945 Tensile deformation *Trans. AIME* **162** 268–90
- [27] Williams J D 2010 Fatigue and fracture mechanics aspects of LIGA fabricated nickel and Ni-20%Fe microstructures *Int. J. Theor. Appl. Multiscale Mech.* **1** 266–79
- [28] Tomkins B 1968 Fatigue crack propagation – an analysis *Phil. Mag.* **18** 1041–66
- [29] Christenson T R, Buchheit T E, Schmale D T and Bourcier R J 1998 Mechanical and metallographic characterization of LIGA fabricated nickel and 80%Ni-20%Fe permalloy *Proc. MRS Symp.* **518** 185–90
- [30] Namazu T and Inoue S 2007 Characterization of single crystal silicon and electroplated nickel films by uniaxial tensile test with in situ x-ray diffraction measurement *Fatigue Fract. Eng. Mater. Struct.* **30** 13–20
- [31] Ludwik P 1909 *Elemente Der Technologischen Mechanik* (Berlin: Springer) pp 32–37
- [32] Matusevich A, Massa J and Mancini R 2013 Computation and uncertainty evaluation of offset yield strength *J. Test. Eval.* **41** 217–30
- [33] Liew L A, Read D T, White R M and Barbosa N 2018 U.S. army ARDEC joint fuze technology program (JFTP) task 2 report: quasi-static tensile tests of microfabricated electrodeposited (LIGA) Ni alloys *NIST Interagency Report* 8182, 2018
- [34] Read D T, Liew L A, White R M, Barbosa N and Geaney J 2019 Measuring flow curve and failure conditions for a MEMS-scale electrodeposited nickel alloy *Mater. Res. Express* **6** 0950a6
- [35] Sharpe W N, LaVan D A and Edwards R L 1997 Mechanical properties of LIGA-deposited nickel for MEMS transducers *Proc. of 1997 Int. Conf. on Solid State Sensors and Actuators (Transducers '97)* pp 607–10

- [36] El-Madhoun Y, Mohamed A and Bassim M N 2004 Cyclic stress-strain behavior of polycrystalline nickel *Mater. Sci. Eng. A* **385** 140–7
- [37] Moser B, Hanlon T, Kumar K S and Suresh S 2006 Cyclic strain hardening of nanocrystalline nickel *Scr. Mater.* **54** 1151–5
- [38] Maass R and Derlet P M 2018 Micro-plasticity and recent insights from intermittent and small-scale plasticity *Acta Mater.* **143** 338–63
- [39] ASM International Handbook Committee 1990 *ASM Handbook Volume 2 Properties and Selection: Nonferrous Alloys and Special Purpose Materials* (Novelty, OH: ASM International)
- [40] Reuss A 1929 Berechnung der fließgrenze von mischkristallen auf grund der plastizitätsbedingung für einkristalle *Z. Angew. Math. Mech.* **9** 49–58
- [41] Voigt W 1910 *Lehrbuch Der Kristallphysik (Mit Ausschluss Der Kristalloptik)* (Leipzig: B G Teubner)
- [42] Krstic V, Erb U and Palumbo G 1993 Effect of porosity on Young's modulus of nanocrystalline materials *Scr. Metall. Mater.* **29** 1501–4
- [43] Schuh C A, Nieh T G and Yamasaki T 2002 Hall-Petch breakdown manifested in abrasive wear resistance of nanocrystalline nickel *Scr. Mater.* **46** 735–40
- [44] Van Swygenhoven H, Caro A and Farkas D 2001 Grain boundary structure and its influence on plastic deformation of polycrystalline FCC metals at the nanoscale: a molecular dynamics study *Scr. Mater.* **44** 1513–6
- [45] Martin M L, Liew L A, Read D, Christenson T, DelRio F and Geaney J 2020 Dominant factors for fracture at the microscale in electrodeposited nickel alloys *Sensors Actuators A* **314** 112239